JACS
JOURNAL OF THE AMERICAN CHEMICAL SOCIETY
pubs.acs.org/JACS
Article

Imparting Ion Selectivity to Covalent Organic Framework Membranes Using *de Novo* Assembly for Blue Energy Harvesting

Sifan Chen, Changjia Zhu, Weipeng Xian, Xinyu Liu, XiaoLong Liu, Qinghua Zhang,* Shengqian Ma, and Qi Sun*

Cite This: *J. Am. Chem. Soc.* 2021, 143, 9415–9422

ABSTRACT: It has long been a challenge to fabricate angstrom-sized functional pores for mimicking the function of biological channels to afford selective transmembrane transport. In this study, we describe a facile strategy to incorporate ionic elements into angstrom-sized channels using *de novo* encapsulation of charged dye molecules during the interface polymerization of a three-dimensional covalent organic framework (3D COF). We demonstrate that this approach is tailorable as it enables control over both the type and content of the guest and thus allows manipulation of the membrane function. The resulting membranes exhibit excellent permselectivity and low membrane resistance, thereby indicating the potential for harvesting salinity gradient (blue) energy. As a proof-of-concept study, the reverse electrodialysis device coupled with positive and negative dye encapsulated COF membranes afforded a power density of up to 51.4 W m^{-2} by mixing the simulated seawater and river water, which far exceeds the commercialization benchmark (5 W m^{-2}). We envision that this strategy will pave the way for constructing new multifunctional biomimetic systems.

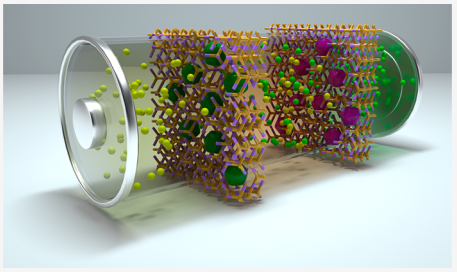

INTRODUCTION

Many natural phenomena involve angstrom-sized functional pores.[1,2] A paradigmatic example is the biological pores in cellular membranes, representing the essential elements in various crucial life processes, such as energy production and storage. A common structural feature shared by these pores is that the selectivity filter regions containing the charged groups are situated on the hydrophobic pore lining.[3,4] To mimic and better understand the sophisticated functions of nature, it is desirable to create artificial channels with similar functional dimensions. However, controllably fabricated angstrom-sized artificial channels have long been a distant goal.[5−13] The advent of reticular chemistry has fundamentally changed the state of affairs as it offers opportunities to construct materials of bespoke pore shape, size, and functionality.[14] Covalent organic frameworks (COFs) with intrinsically hydrophobic order pore channels offer a compelling opportunity to mimic the function of biological channels.[15−35] However, despite the promise of synthetic flexibility in terms of pore structure and environment, direct fabrication of ionic COFs with the angstrom-sized pores remains a challenge.[36,37] Thus, to develop the application of COF chemistry to mimic the function of ionic biological channels, a new strategy to functionalize the COF membrane is required.

Host−guest assemblies have been a versatile platform for a broad spectrum of applications including catalysis, sensors, and biorelated applications.[38−42] *De novo* encapsulation of functional species into the host materials during their synthesis is useful for generating functional materials such as biocomposites, which are otherwise inaccessible or impossible to achieve directly. Moreover, the host components self-assemble around the functional species encapsulating them within a porous matrix, which requires neither particular host porous materials nor guest molecules. This allows fundamental investigation of multiple-level control over the interplay between hosts and guests.[43,44] Given these properties, we envisioned that encapsulating the ionic molecules during the assembly of COF membranes offers a promising solution, which also circumvents the lengthy synthetic procedures or incompatible crystallization conditions.

Owing to the abundance and relatively large size of dyes,[45,46] which can be held in the framework matrix with angstrom-sized apertures, we sought to immobilize the charged dye molecules to create COF-based ionic channels, but in principle, various types of functional molecules can be encapsusulated. To maximize the impact of the framework, a three-dimensional (3D) confinement is preferred over one-dimensional (1D) pore infiltration, as the blocked or partially blocked pores by the guest molecules can be alleviated.[47,48] Therefore, we propose a proof-of-concept synthesis of dye-encapsulated COF membranes through an interface-driven

Received: February 23, 2021
Published: May 24, 2021

https://doi.org/10.1021/jacs.1c02090
J. Am. Chem. Soc. 2021, 143, 9415−9422

assembly and polymerization strategy. The successful implementation of this strategy was demonstrated by encapsulating the various dye molecules into the robust 3D COF membrane, COF-300. Given that a large amount of energy is available from the salinity difference, they can be harvested via membrane-based reverse electrodialysis (RED), which, with massive parallelization, could work as a useful nonconventional energy source.[49−61] To curb the undesired mixing of river water and seawater and thereby the power generation efficiency, a major challenge is building nanochannels with high permselectivity. Therefore, to test the applicability of the created ionic nanochannels, we evaluated their performance in harvesting osmotic energy. Because of the well-defined angstrom-sized ionic channels, the resulting membranes exhibited high permselectivity, up to a salinity ratio of 1 M/0.1 mM. Given the general applicability of this strategy, both anionic and cationic nanochannels can be created (Figure 1).

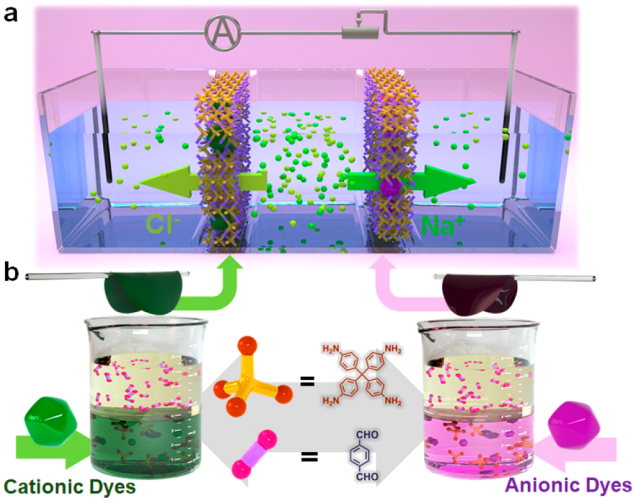

Figure 1. Conceptual scheme. (a) Diagrammatic sketch of a pair of the cation- and anion-selective membranes mounted in a three-compartment conductive cell to harvest osmotic energy. (b) Bottom-up assembly of ionic dye modified COF-based nanofluidic membranes. Oppositely charged COF membrane pairs can be readily obtained by encapsulating positively and negatively charged dye molecules, respectively.

The output power density of the RED stack assembled by positively and negatively charged dye@COF membranes reached 51.4 W m^{-2} by mixing simulated seawater (0.5 M NaCl) and river water (0.01 M NaCl), which is more than 10-fold greater than the commercialization benchmark and places it among the best developed nanofluidic osmotic power generators (Table S1). These findings provide a powerful and straightforward way to construct artificial ionic channels.

RESULTS AND DISCUSSION

Membrane Preparation and Characterization. COF-300 was selected as an immobilization matrix because of its high chemical stability and angstrom-sized pores (7.2 Å), which are smaller than numerous dye molecules.[62] This prevented the encapsulated dyes from leaching. Enveloping dye molecules in the COF-300 membrane was accomplished using *de novo* assembly. As schematically illustrated in Figure 1b, a terephthalaldehyde organic solution was layered onto the tetraphenylmethaneamine-dye−acidic acid aqueous solution for 3 days at 35 °C. During the interface polymerization, the conjugated dye molecules can be readily absorbed by the COF layers via $\pi-\pi$ interactions, guaranteeing strong physical adsorption forces for dye loading (Figure S1). The dye molecules were therefore embedded within the COF matrix. The resulting membrane was washed sequentially with ethanol and water to remove the unreacted monomers and dye molecules that may have remained weakly adsorbed on the outer surface of the membrane. The presence of dye molecules within the COF membrane could be directly observed by the resulting color change from yellow to the corresponding dye color (Figure S2). Both cationic and anionic dyes could be successfully immobilized, demonstrating the general applicability of this strategy. In addition, the dye content in the resulting membranes can be readily adjusted by varying the concentration of the aqueous dye solution. As a representative sample among the synthesized dye-encapsulated COF membranes, the membranes bearing Janus green B, a positively charged dye molecule (JG_x@COF, where x refers to the content of Janus green B (JG) in the resulting membranes), have been illustrated in detail. In addition, to confirm the critical role of the encapsulated dye molecules in their subsequent ion screening performance, the COF-300 membrane was fabricated for comparison (Figures S3−S5).

The successful formation of COF-300 and immobilization of JG in the membrane were supported using the Fourier transform infrared (FT-IR) spectra. The appearance of a characteristic imine stretching vibration band at 1620 cm^{-1} validates the occurrence of amine-aldehyde condensation to imine linkages.[62] Meanwhile, a new band at 1590 cm^{-1} originating from the JG (C═C stretching mode) was observed in the spectra of JG_x@COF with an increase in the concentration of the JG solution. Notably, the absorbance corresponding to aldehyde C═O (1690 cm^{-1}) and amine N−H bonds (3200 cm^{-1}) of the starting materials, lacking in the COF-300 membrane, appeared in the spectra of JG_x@COF and became stronger as the JG content increased. This can be rationalized, as the dye molecule is larger than the pore size of COF-300, which prevents full condensation of the monomers (Figures S6 and S7). The exact content of JG in the resulting membranes was determined using ultraviolet−visible spectroscopy (UV−vis) of the digested samples, with $JG_{4.2}$@COF, $JG_{24.2}$@COF, $JG_{80.1}$@COF, and $JG_{117.6}$@COF referring to the dye content of 4.2, 24.2, 80.1, and 117.6 mg g^{-1}, respectively (Figure S8). The homogeneous distribution of JG in the resulting membrane was revealed using laser scanning confocal microscopy (LSCM) with an excitation wavelength of 405 nm, where characteristic fluorescence of JG was observed across the entire membrane (Figure S9). The introduction of ionic sites on the backbone is usually accompanied by water uptake, a side effect that results in the ionic membrane swelling, which is detrimental to their long-term run stability. In our case, the dye molecules were embedded in the rigid COF framework, and the membrane swelling resulting from water adsorption could be significantly depressed (Figure S10).

To increase the processing stability of the membranes, we grew them on a polyacrylonitrile (PAN) ultrafiltration membrane (Figure S11). As shown in Figures S12−S17, high-quality membranes could be grown on the surface of PAN with the resulting thicknesses of the spongy top layer ranging from 190 to 215 nm. Water contact angle (WCA) measurements revealed that these membranes are hydrophobic, with WCA values ranging from 104.3° to 92.1° (Figure S18). The ζ

https://doi.org/10.1021/jacs.1c02090
J. Am. Chem. Soc. 2021, 143, 9415−9422

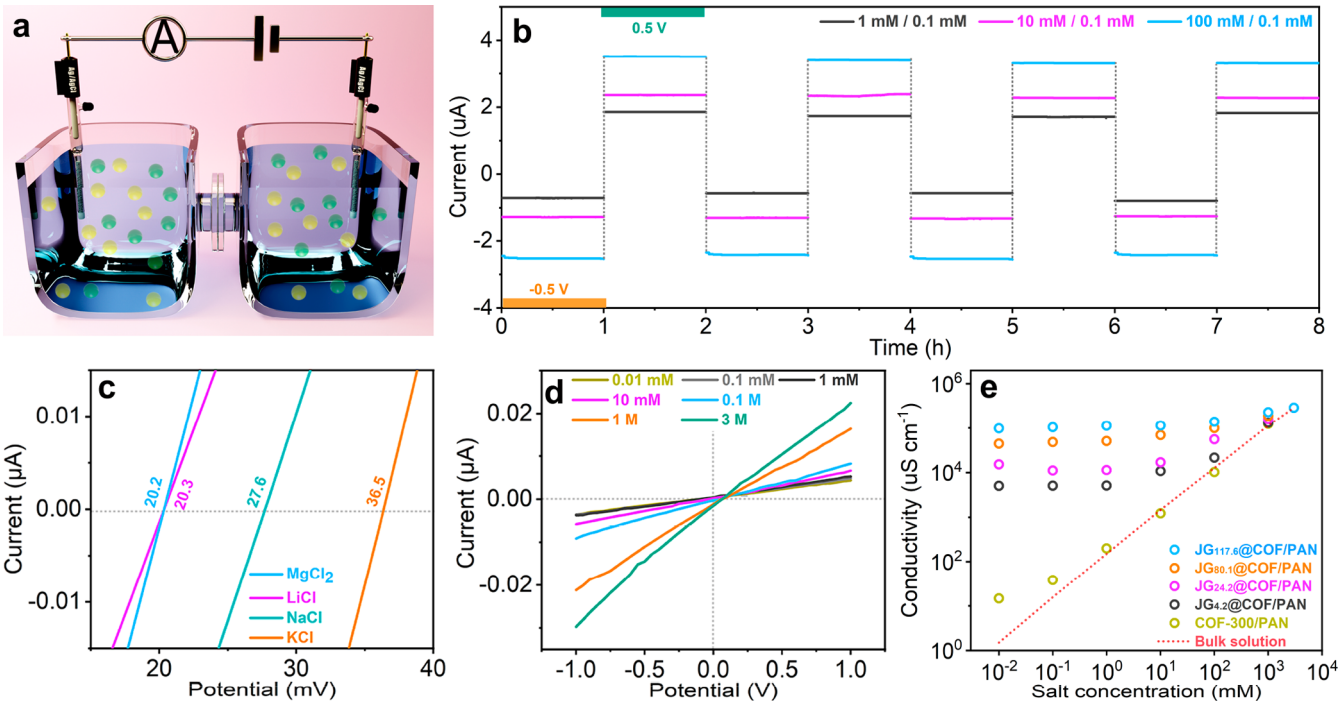

Figure 2. Investigation of ion transport stability and property of JG_x@COF/PAN. (a) Schematic illustration of the experimental setup for measuring the transmembrane ionic transport (cation, green; anion, yellow). (b) $I-T$ curves of $JG_{80.1}$@COF/PAN recorded in various concentration gradients KCl electrolytes with an external bias alternating between +0.5 V and −0.5 V to investigate the stability of the membrane with each cycle lasting for 8 h. (c) $I-V$ plots recorded for $JG_{80.1}$@COF/PAN in various salt solutions having a concentration ratio of 0.1 M/1 mM. (d) $I-V$ plots for $JG_{80.1}$@COF/PAN recorded in KCl electrolytes with concentrations ranging from 0.01 mM to 3 M. (e) Conductivity versus KCl concentration for JG_x@COF/PAN. The ionic conductivity deviates from the bulk value (dashed line) in the low-concentration region, suggestive of surface-charge governed ion transport.

potential measurements on JG_x@COF/PAN consistently suggested that the COF active layers were positively charged, with the values increasing in response to an increase in the JG content (Figure S19). Tests for membrane leakage were carried out using dye removal from water. Rhodamine B, a positively charged dye molecule with a diameter of 1.58 × 1.36 nm, could be fully cut off by the JG_x@COF membrane, as evidenced by the fact that no dye in the filtrate was detected by UV−vis and the increased dye concentration in the feed solution after dead-end filtration (see details in the experimental section and Figures S20 and S21). To further confirm the defect less of the membrane, $MgCl_2$ rejection experiments were carried out, considering that the size of hydrated Mg^{2+} ion is 8.5 Å, slightly larger than that of the pore size of COF-300, which showed that 96% of $MgCl_2$ solute can be excluded (Figure S22).

Investigation of Transmembrane Ion Transport. With the ionic membranes available, we investigated their potential applications. The ever-growing energy demands have motivated the exploration of nonconventional energy. Salinity gradient energy in the form of Gibbs free energy has been recognized as a sustainable energy source. Inspired by the advanced skills of some living organisms to convert intracellular osmotic energy into potentials enabled by ion channels (an electric eel can generate electric shocks up to 600 V by linking stacks of electrolytes in series[63]), enormous scientific research on ion-channel-mimetic nanofluidic membrane-based RED to capture this energy has been comprehensively investigated. The obstacles that impede the practical application of this technology are the uncontrolled mixing and high membrane resistance.[49−62]

We first evaluated the stability of dye@COF/PAN for ion transport. To do so, the membrane was squeezed between two fluid reservoirs filled with various concentrations of symmetric KCl solutions (Figure 2a). Ag/AgCl electrodes were employed to measure the electric current passing through the membranes. Current−time ($I-T$) plots were recorded by alternatively applying a bias of +0.5 V/−0.5 V to various electrolytes, and a total period of 24 h was collected with each cycle lasting for 8 h. This revealed that both the positive and negative currents were constant over various salt concentrations, indicative of the stable transmembrane ion transport (Figure 2b). Furthermore, no dye leaching was observed throughout this process.

To understand the ion transport behavior, molecular dynamics (MD) simulations were performed, which showed that only Cl^- ions can translocate from the KCl aqueous solution to the COF layers, suggestive of the higher transport activity of anions than that of cations through JG_x@COF (Figure S23). To quantitatively determine the charge selectivity of JG_x@COF, reversal potentials (V_{rev}) of various electrolytes ($MgCl_2$, LiCl, NaCl, and KCl) were measured. Asymmetric salt solutions with a concentration gradient of 0.1 M/1 mM were applied with the COF active layer facing the high concentration side. The x-intercepts of the current−voltage ($I-V$) plots afforded V_{rev} values of 20.2 mV, 20.3 mV, 27.6 mV, and 36.5 mV for $MgCl_2$, LiCl, NaCl, and KCl, respectively, indicating that the membrane was anion-selective (Figure 2c). According to the Goldman−Hodgin−Katz equation, the permeability ratios of chloride ion to metal ion were calculated to be 1357, 452, 296, and 189 for $MgCl_2$, LiCl, NaCl, and KCl, respectively.[64]

https://doi.org/10.1021/jacs.1c02090
J. Am. Chem. Soc. 2021, 143, 9415−9422

Next, we investigated the transmembrane ionic transport properties of the composite membranes. The $I-V$ measurements were conducted over a wide range of symmetric KCl solutions. KCl was selected as a representative electrolyte because K^+ and Cl^- showed comparable bulk mobilities and thus exhibited negligible liquid junction potentials.[65] The $I-V$ plots recorded in KCl solutions with concentrations ranging from 0.01 mM to 3 M exhibited ohmic behavior (Figure 2d). The plots of the conductivity of JG_x@COF/PAN versus KCl concentrations revealed that the transmembrane conductivities significantly deviated from the bulk value (dashed line) when the KCl concentration was lower than 1 M, indicating that the ion transport through the membranes was predominantly surface-charge governed (Figure 2e). By sharp contrast, conductivities of COF-300/PAN approach the bulk conduction value, with values proportional to the corresponding KCl concentration. These phenomena can be reasonably ascribed to the electrostatic effects of the encapsulated ionic dye molecules on the fluid. Charged surfaces in contact with electrolytes repel co-ions while attracting counterions to form electric double layers (EDLs), which screen the net and immobilized surface-charge density. The requirement of charge neutrality implies that the number of mobile counterions in the membrane will exceed the contribution of bulk ions and thus dominate transport. Therefore, the ion conductivity in JG_x@COF/PAN exceeded that in the noncharged channels by orders of magnitude, and the measured conductivities deviated from the bulk value more significantly from bottom to top along with modulation of the JG content in the membrane from 0 to 117.6 mg g^{-1}.[66,67]

To measure the permselectivity of JG_x@COF/PAN quantitatively for achieving an optimal dye percentage to maximize the RED energy conversion efficiency, $I-V$ curves were recorded under a wide range of KCl concentration differences across the membranes. To eliminate the potential generated from redox reactions on the electrodes in different KCl concentrations, an in-house conductive cell with three fluid reservoirs was used, whereby the KCl concentration of the two side reservoirs was fixed at 0.1 mM while that in the middle reservoir increased from 1 mM to 1 M (Figure 3a). An example plot of open-circuit voltage (V_{oc}) and short-circuit current (I_{sc}) versus concentration gradients for $JG_{80.1}$@COF/PAN is shown in Figure 3b. Given that I_{sc} is produced only if one ion diffuses at a higher rate than the other through the pore, the detected I_{sc} confirmed the discrepancy in the transmembrane activity of K^+ and Cl^-. Because of ion-selective accumulation, transmembrane potentials were generated, which followed a trend similar to that of I_{sc} in response to the concentration differences, showing an increasing and then a decreasing trend. The V_{oc} peaked at a concentration gradient of 0.5 M/0.1 mM (Figure S24). To calculate the ionic charge selectivity quantitatively, the transference number (t_-) under different salinity gradients was calculated using the following equation:

$$t_- = \frac{1}{2}\left(\frac{V_{oc}F}{RT \ln \frac{a_{HC}}{a_{LC}}} + 1\right)$$

where a_{HC}, a_{LC}, F, R, and T are the activities of high concentration and low concentration solutions, Faraday constant, gas constant, and temperature, respectively. Figure 3c shows the t_- values as a function of the concentration

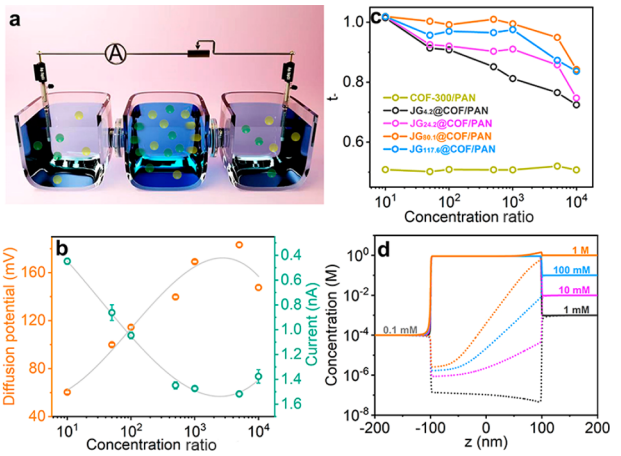

Figure 3. Investigation of permselectivity of JG_x@COF/PAN. (a) Schematic illustration of the experimental setup used to evaluate the permselectivity of the membranes (cation, green; anion, yellow). (b) Plots of the recorded V_{oc} and I_{sc} versus various KCl concentration difference across $JG_{80.1}$@COF/PAN. The KCl concentration of the side reservoirs was set to 0.1 mM. (c) Plots of transference number (t_-) versus various KCl concentration difference across JG_x@COF/PAN. (d) Numerical simulation of the distribution of Cl^- (solid line) and K^+ (dashed line) and in the nanochannels of $JG_{80.1}$@COF/PAN.

gradient of JG_x@COF/PAN, which reveals that the charged dye content has a significant impact on the ion screening capability of the membrane. COF-300/PAN shows negligible ion screening ability, giving rise to t_+ values close to 0.5. The slight cation transport selectivity is owing to the negative charge of PAN. Introducing JG resulted in significantly improved permselectivity. $JG_{4.2}$@COF/PAN with a dye content of 4.2 mg g^{-1} exhibited a sharp increase in permselectivity, generating a t_- value of 0.77 even at a very high concentration gradient of 0.5 M/0.1 mM. By increase of the dye weight content from 4.2 mg g^{-1} to 80.1 mg g^{-1}, the ion screening performance over the tested concentration gradient ranges gradually improved; with further increasing of the dye weight content to 117.6 mg g^{-1}, a slight decrease in selectivity was observed. To explain these phenomena, we reasoned that at low dye content, the ionic channels are not continued; however, too many dye molecules inevitably result in defects in the crystalline matrix, which are deleterious to screening ions. The optimal material $JG_{80.1}$@COF/PAN exclusively transports Cl^- when the concentration gradients are smaller than 0.1 M/0.1 mM, affording a t_- value close to 1. By further increase of the concentration difference to 10 000-fold, the t_- value is still maintained at 0.84. The decrease in permselectivity is because EDL is attenuated in high electrolyte concentrations, which weakens the surface-charge governed ionic transport (Table S2).

To gain additional insight into ion transport in these membranes, numerical simulations based on steady-state Poisson–Nernst–Plank (PNP) equations were carried out. A 2D model with 0.72 nm width and 200 nm length was employed to simulate the fluidic pathway (Figure S24). The charge density of the inner channel surface was varied from 0 to 52.2 mC m^{-2} (Table S3). To simulate the salinity gradient, the KCl concentration in the left reservoir was fixed at 0.1 mM, and that in the right reservoir was varied from 1 mM to 1 M. The ion distribution profiles in response to the salinity gradient showed that the concentration of Cl^- ions was significantly higher than that of K^+ ions, although the ratio decreased with

https://doi.org/10.1021/jacs.1c02090
J. Am. Chem. Soc. 2021, 143, 9415–9422

an increase in the concentration gradient, validating the experimental trends (Figures 3d, S25, and S26).

Osmotic Energy Harvesting. The high permselectivity of these membranes prompted us to investigate their osmotic energy conversion efficiency. To harvest the energy continuously from salinity gradients via the net diffusion current, an RED device is usually designed by assembling alternating anion-exchange membranes and cation-exchange membranes. Therefore, we coupled $HB_{67.7}$@COF/PAN, an anionic dye (hydroxynaphthol blue) encapsulated COF-300 membrane, with $JG_{80.1}$@COF/PAN. The generated power can be exported by supplying an external load resistor (R_L). A standard simulated seawater (0.5 M NaCl) and river water (0.01 M NaCl) solution was applied, and four configurations were arranged to optimize the osmotic energy conversion efficiency by manipulating the order of solutions and the orientation of membranes (Figure S27). The highest output power density was achieved when the middle reservoir of a three-compartment conductive cell was filled with 0.5 M NaCl and the two-side reservoirs were filled with 0.01 M NaCl, and the COF layers faced the low concentration side. With the increase in R_L, the diffusion current gradually decreased; however, the output power density peaked at R_L of 14 kΩ (Figure 4a).

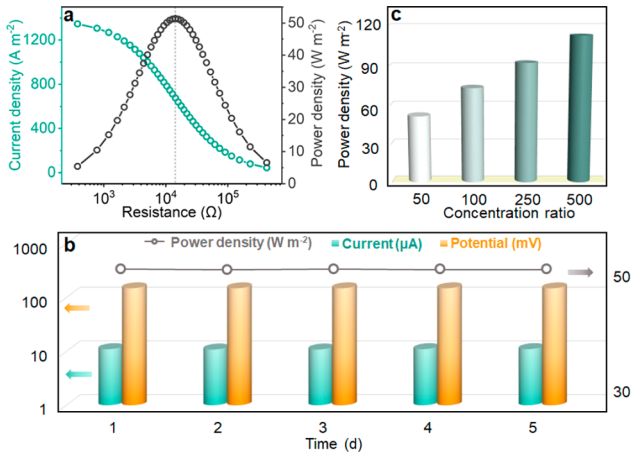

Figure 4. Performance of the RED device assembled by dye@COF/PAN membranes. (a) The power was output to an external circuit to supply an electronic load. The diffusion current of the RED device decreased with increasing load resistance, and the output power reached its peak at ≈14 kΩ by mixing simulated river water and seawater. (b) Plots of V_{oc}, I_{sc}, and output power density of the RED device over time. (c) Theoretically extractable energy from the mixing of a dilute stream with saline solutions.

Calculated according to $P_{out} = I^2 \times R_L$, the power density of 51.4 W m^{-2} can be obtained (see the equivalent circuit diagram in Figure S28); this is more than10-fold superior to the commercialization benchmark (~5 W m^{-2}), ranking the system among the best developed systems. Previous research has proven that the extractable power density reaches its maximum when R_L is equal to the membrane resistance, thus suggesting that the internal resistance of dye@COF pairs is 14 kΩ, which represents one of the lowest values ever reported for membrane systems. Notably, the RED device afforded a V_{oc} value of 150 mV, corresponding to an energy conversion efficiency of 36.8%, which exceeds most of the state-of-the-art membranes. Operational stability is one of the key properties of all systems for practical applications. We thus conducted a long-term stability test for the resulting COF-based RED stack, showing that the current and transmembrane potential did not decline for at least 5 days (Figures 4b and S29).

To further extend the applicability of the developed RED devices, we estimated the salinity gradient power from a series of solutions with different concentrations, given that in addition to the salinity difference at the river mouth, brines generated by desalination plants could also be used to harvest energy. To evaluate the output power density of the dye@COF/PAN RED device, the salt solution of the two-side reservoirs was maintained at 10 mM and the salt concentration of the middle reservoir was increased from 0.5 to 5 M. The output power density was increased from 51.4 to 112.3 W m^{-2} as the salinity ratio increased from 50- to 500-fold (Figures 4c and S30).

CONCLUSION

In summary, we presented a general and straightforward strategy to construct angstrom-sized ionic channels, as demonstrated by *de novo* incorporation of ionic dye molecules during the assembly of COF membranes. Given that the size of encapsulated dyes is larger than that of the pore aperture of COF-300, the resulting functional membranes are very stable and suitable for use as platforms in biomimic processes. The accommodated dye molecules impart the membrane with outstanding ion screening ability, as validated by the pristine COF-300 exhibiting negligible permselectivity (Figure S31). With these attributes, the RED stack, assembled by cationic and anionic dye molecules encapsulated membranes, exhibits excellent performance in harvesting osmotic energy, placing it within striking distance of the all-time best RED membrane-based system in terms of power density. We believe that this strategy integrated with the control over the topology, pore structure, and chemistry offered by COFs would provide new opportunities to mimic the sophisticated functions of biological channels.

ASSOCIATED CONTENT

Supporting Information

The Supporting Information is available free of charge at https://pubs.acs.org/doi/10.1021/jacs.1c02090.

Materials synthesis, characterization details, supporting data items, and supporting figures (PDF)

AUTHOR INFORMATION

Corresponding Authors

Qinghua Zhang − *Zhejiang Provincial Key Laboratory of Advanced Chemical Engineering Manufacture Technology, College of Chemical and Biological Engineering, Zhejiang University, Hangzhou 310027, China;* orcid.org/0000-0003-1350-6388; Email: qhzhang@zju.edu.cn

Qi Sun − *Zhejiang Provincial Key Laboratory of Advanced Chemical Engineering Manufacture Technology, College of Chemical and Biological Engineering, Zhejiang University, Hangzhou 310027, China;* orcid.org/0000-0002-1698-8741; Email: sunqichs@zju.edu.cn

Authors

Sifan Chen − *Zhejiang Provincial Key Laboratory of Advanced Chemical Engineering Manufacture Technology, College of Chemical and Biological Engineering, Zhejiang University, Hangzhou 310027, China*

Changjia Zhu − *Zhejiang Provincial Key Laboratory of Advanced Chemical Engineering Manufacture Technology, College of Chemical and Biological Engineering, Zhejiang University, Hangzhou 310027, China; Department of Chemistry, University of North Texas, Denton, Texas 76201, United States*

Weipeng Xian − *Zhejiang Provincial Key Laboratory of Advanced Chemical Engineering Manufacture Technology, College of Chemical and Biological Engineering, Zhejiang University, Hangzhou 310027, China*

Xinyu Liu − *School of Materials, Sun Yat-Sen University, Guangzhou 510006, China*

XiaoLong Liu − *School of Materials, Sun Yat-Sen University, Guangzhou 510006, China;* orcid.org/0000-0002-7346-7846

Shengqian Ma − *Department of Chemistry, University of North Texas, Denton, Texas 76201, United States;* orcid.org/0000-0002-1897-7069

Complete contact information is available at: https://pubs.acs.org/10.1021/jacs.1c02090

Author Contributions

The manuscript was written through contributions of all authors. All authors have given approval to the final version of the manuscript.

Notes

The authors declare no competing financial interest.

■ ACKNOWLEDGMENTS

The authors acknowledge the National Science Foundation of China (Grants 22072132, 21776249, and 21878267)

■ REFERENCES

(1) Gouaux, E.; MacKinnon, R. Principles of selective ion transport in channels and pumps. *Science* **2005**, *310*, 1461−1465.

(2) Esfandiar, A.; Radha, B.; Wang, F. C.; Yang, Q.; Hu, S.; Garaj, S.; Nair, R. R.; Geim, A. K.; Gopinadhan, K. Size effect in ion transport through angstrom-scale slits. *Science* **2017**, *358*, 511−513.

(3) Tagliazucchi, M.; Peleg, O.; Kröger, M.; Rabin, Y.; Szleifer, I. Effect of charge, hydrophobicity, and sequence of nucleoporins on the translocation of model particles through the nuclear pore complex. *Proc. Natl. Acad. Sci. U. S. A.* **2013**, *110*, 3363−3368.

(4) Fornasiero, F.; Park, H. G.; Holt, J. K.; Stadermann, M.; Grigoropoulos, C. P.; Noy, A.; Bakajin, O. Ion exclusion by sub-2-nm carbon nanotube pores. *Proc. Natl. Acad. Sci. U. S. A.* **2008**, *105*, 17250−17255.

(5) Lu, J.; Zhang, H.; Hou, J.; Li, X.; Hu, X.; Hu, Y.; Easton, C. D.; Li, Q.; Sun, C.; Thornton, A. W.; Hill, M. R.; Zhang, X.; Jiang, G.; Liu, J. Z.; Hill, A. J.; Freeman, B. D.; Jiang, L.; Wang, H. Efficient metal ion sieving in rectifying subnanochannels enabled by metal-organic frameworks. *Nat. Mater.* **2020**, *19*, 767−774.

(6) Shehzad, M. A.; Wang, Y.; Yasmin, A.; Ge, X.; He, Y.; Liang, X.; Zhu, Y.; Hu, M.; Xiao, X.; Ge, L.; Jiang, C.; Yang, Z.; Guiver, M. D.; Wu, L.; Xu, T. Biomimetic nanocones that enable high ion permselectivity. *Angew. Chem.* **2019**, *131*, 12776−12784.

(7) Tan, R.; Wang, A.; Malpass-Evans, R.; Williams, R.; Zhao, E. W.; Liu, T.; Ye, C.; Zhou, X.; Darwich, B. P.; Fan, Z.; Turcani, L.; Jackson, E.; Chen, L.; Chong, S. Y.; Li, T.; Jelfs, K. E.; Cooper, A. I.; Brandon, N. P.; Grey, C. P.; McKeown, N. B.; Song, Q. Hydrophilic microporous membranes for selective ion separation and flow-battery energy storage. *Nat. Mater.* **2020**, *19*, 195−202.

(8) Xu, Y. Nanofluidics: a new arena for materials science. *Adv. Mater.* **2018**, *30*, 1702419.

(9) Tagliazucchi, M.; Szleifer, I. Transport mechanisms in nanopores and nanochannels: can we mimic nature? *Mater. Today* **2015**, *18*, 131−142.

(10) Jiang, Z.-Y.; Liu, H.-L.; Ahmed, S. A.; Hanif, S.; Ren, S.-B.; Xu, J.-J.; Chen, H.-Y.; Xia, X.-H.; Wang, K. Insight into ion transfer through the sub-nanometer channels in zeolitic imidazolate frameworks. *Angew. Chem., Int. Ed.* **2017**, *56*, 4767−4771.

(11) Xiao, K.; Chen, L.; Zhang, Z.; Xie, G.; Li, P.; Kong, X.-Y.; Wen, L.; Jiang, L. A tunable ionic diode based on a biomimetic structure-tailorable nanochannel. *Angew. Chem., Int. Ed.* **2017**, *56*, 8168−8172.

(12) Wang, J.; Zhang, Z.; Zhu, J.; Tian, M.; Zheng, S.; Wang, F.; Wang, X.; Wang, L. Ion sieving by a two-dimensional $Ti_3C_2T_x$ alginate lamellar membrane with stable interlayer spacing. *Nat. Commun.* **2020**, *11*, 3540.

(13) Martin, C. R.; Siwy, Z. S. Learning nature's way: biosensing with synthetic nanopores. *Science* **2007**, *317*, 331−332.

(14) Yaghi, O. M.; Kalmutzki, M. J.; Diercks, C. S. *Introduction to Reticular Chemistry: Metal-Organic Frameworks and Covalent Organic Frameworks*; Wiley-VCH: Hoboken, NJ, U.S., 2019; pp 1−509.

(15) Song, Y.; Sun, Q.; Aguila, B.; Ma, S. Opportunities of covalent organic frameworks for advanced applications. *Adv. Sci.* **2019**, *6*, 1801410.

(16) Slater, A. G.; Cooper, A. I. Function-led design of new porous materials. *Science* **2015**, *348*, aaa8075.

(17) Lohse, M. S.; Bein, T. Covalent organic frameworks: structures, synthesis, and applications. *Adv. Funct. Mater.* **2018**, *28*, 1705553.

(18) Kandambeth, S.; Dey, K.; Banerjee, R. Covalent organic frameworks: chemistry beyond the structure. *J. Am. Chem. Soc.* **2019**, *141*, 1807−1822.

(19) Jin, Y.; Hu, Y.; Zhang, W. Tessellated multiporous two-dimensional covalent organic frameworks. *Nat. Rev. Chem.* **2017**, *1*, 0056.

(20) Han, X.; Yuan, C.; Hou, B.; Liu, L.; Li, H.; Liu, Y.; Cui, Y. Chiral covalent organic frameworks: design, synthesis and property. *Chem. Soc. Rev.* **2020**, *49*, 6248−6272.

(21) Guan, X.; Chen, F.; Fang, Q.; Qiu, S. Design and applications of three dimensional covalent organic frameworks. *Chem. Soc. Rev.* **2020**, *49*, 1357−1384.

(22) Geng, K.; He, T.; Liu, R.; Dalapati, S.; Tan, K. T.; Li, Z.; Tao, S.; Gong, Y.; Jiang, Q.; Jiang, D. Covalent organic frameworks: design, synthesis, and functions. *Chem. Rev.* **2020**, *120*, 8814−8933.

(23) Evans, A. M.; Parent, L. R.; Flanders, N. C.; Bisbey, R. P.; Vitaku, E.; Kirschner, M. S.; Schaller, R. D.; Chen, L. X.; Gianneschi, N. C.; Dichtel, W. R. Seeded growth of single-crystal two-dimensional covalent organic frameworks. *Science* **2018**, *361*, 52−57.

(24) Liu, H.; Chu, J.; Yin, Z.; Cai, X.; Zhuang, L.; Deng, H. Covalent organic frameworks linked by amine bonding for concerted electrochemical reduction of CO_2. *Chem.* **2018**, *4*, 1696−1709.

(25) Dong, J.; Zhang, K.; Li, X.; Qian, Y.; Zhu, H.; Yuan, D.; Xu, Q.-H.; Jiang, J.; Zhao, D. Ultrathin two-dimensional porous organic nanosheets with molecular rotors for chemical sensing. *Nat. Commun.* **2017**, *8*, 1142.

(26) Colson, J. W.; Woll, A. R.; Mukherjee, A.; Levendorf, M. P.; Spitler, E. L.; Shields, V. B.; Spencer, M. G.; Park, J.; Dichtel, W. R. Oriented 2D covalent organic framework thin films on single-layer graphene. *Science* **2011**, *332*, 228−231.

(27) Kandambeth, S.; Biswal, B. P.; Chaudhari, H. D.; Rout, K. C.; Kunjattu H., S.; Mitra, S.; Karak, S.; Das, A.; Mukherjee, R.; Kharul, U. K.; Banerjee, R. Selective molecular sieving in self-standing porous covalent-organic-framework membranes. *Adv. Mater.* **2017**, *29*, 1603945.

(28) Yuan, C.; Wu, X.; Gao, R.; Han, X.; Liu, Y.; Long, Y.; Cui, Y. Nanochannels of covalent organic frameworks for chiral selective transmembrane transport of amino acids. *J. Am. Chem. Soc.* **2019**, *141*, 20187−20197.

(29) Hao, Q.; Li, Z.-J.; Lu, C.; Sun, B.; Zhong, Y.-W.; Wan, L.-J.; Wang, D. Oriented two-dimensional covalent organic framework films for near-infrared electrochromic application. *J. Am. Chem. Soc.* **2019**, *141* (50), 19831−19838.

(30) Yang, H.; Yang, L.; Wang, H.; Xu, Z.; Zhao, Y.; Luo, Y.; Nasir, N.; Song, Y.; Wu, H.; Pan, F.; Jiang, Z. Covalent organic framework membranes through a mixed-dimensional assembly for molecular separations. *Nat. Commun.* **2019**, *10*, 2101.
(31) Zhao, Y.; Guo, L.; Gándara, F.; Ma, Y.; Liu, Z.; Zhu, C.; Lyu, H.; Trickett, C. A.; Kapustin, E. A.; Terasaki, O.; Yaghi, O. M. A synthetic route for crystals of woven structures, uniform nanocrystals, and thin films of imine covalent organic frameworks. *J. Am. Chem. Soc.* **2017**, *139*, 13166−13172.
(32) Shinde, D. B.; Sheng, G.; Li, X.; Ostwal, M.; Emwas, A.-H.; Huang, K.-W.; Lai, Z. Crystalline 2D covalent organic framework membranes for high-flux organic solvent nanofiltration. *J. Am. Chem. Soc.* **2018**, *140*, 14342−14349.
(33) Fu, J.; Das, S.; Xing, G.; Ben, T.; Valtchev, V.; Qiu, S. Fabrication of COF-MOF composite membranes and their highly selective separation of H_2/CO_2. *J. Am. Chem. Soc.* **2016**, *138*, 7673−7680.
(34) Li, Y.; Wu, Q.; Guo, X.; Zhang, M.; Chen, B.; Wei, G.; Li, X.; Li, X.; Li, S.; Ma, L. Laminater self-standing covalent organic framework membrane with uniformly distributed subnanopores for ionic and molecular sieving. *Nat. Commun.* **2020**, *11*, 599.
(35) Sasmal, H. S.; Halder, A.; Kunjattu H, S.; Dey, K.; Nadol, A.; Ajithkumar, T. G.; Bedadur, P. R.; Banerjee, R. Covalent self-assembly in two dimensions: connecting covalent organic framework nanospheres into crystalline and porous thin films. *J. Am. Chem. Soc.* **2019**, *141*, 20371−20378.
(36) Lu, Q.; Ma, Y.; Li, H.; Guan, X.; Yusran, Y.; Xue, M.; Fang, Q.; Yan, Y.; Qiu, S.; Valtchev, V. Postsynthetic functionalization of three-dimensional covalent organic framework for selective extraction of lanthanide ions. *Angew. Chem., Int. Ed.* **2018**, *57*, 6042−6048.
(37) Li, Z.; Li, H.; Guan, X.; Tang, J.; Yusran, Y.; Li, Z.; Xue, M.; Fang, Q.; Yan, Y.; Valtchev, V.; Qiu, S. Three-dimensional ionic covalent organic frameworks for rapid, reversible, and selective ion exchange. *J. Am. Chem. Soc.* **2017**, *139*, 17771−17774.
(38) Chen, B.; Xiang, S.; Qian, G. Metal-organic frameworks with functional pores for recognition of small molecules. *Acc. Chem. Res.* **2010**, *43*, 1115−1124.
(39) Li, P.; Modica, J. A.; Howarth, A. J.; Vargas L., E.; Moghadam, P. Z.; Snurr, R. Q.; Mrksich, M.; Hupp, J. T.; Farha, O. K. Toward design rules for enzyme immobilization in hierarchical mesoporous metal-organic frameworks. *Chem.* **2016**, *1*, 154−169.
(40) Shieh, F.-K.; Wang, S.-C.; Yen, C.-I.; Wu, C.-C.; Dutta, S.; Chou, L.-Y.; Morabito, J. V.; Hu, P.; Hsu, M.-H.; Wu, K. C.-W.; Tsung, C.-K. Imparting functionality to biocatalysts via embedding enzymes into nanoporous materials by a *de novo* approach: size-selective sheltering of catalase in metal-organic framework microcrystals. *J. Am. Chem. Soc.* **2015**, *137*, 4276−4279.
(41) Park, J.; Wang, Z. U.; Sun, L.-B.; Chen, Y.-P.; Zhou, H.-C. Introduction of functionalized mesopores to metal-organic frameworks *via* metal-ligand-fragment coassembly. *J. Am. Chem. Soc.* **2012**, *134*, 20110−20116.
(42) Sun, Q.; Pan, Y.; Wang, X.; Li, H.; Farmakes, J.; Aguila, B.; Yang, Z.; Ma, S. Mapping out the degree of freedom of hosted enzymes in confined spatial environments. *Chem.* **2019**, *5*, 3184−3195.
(43) Guo, Y.; Ying, Y.; Mao, Y.; Peng, X.; Chen, B. Polystyrene sulfonate threaded through a metal-organic framework membrane for fast and selective lithium-ion separation. *Angew. Chem., Int. Ed.* **2016**, *55*, 15120−15124.
(44) Guo, Y.; Jiang, Z.; Ying, W.; Chen, L.; Liu, Y.; Wang, X.; Jiang, Z.-J.; Chen, B.; Peng, X. A DNA-threaded ZIF-8 membrane with high proton conductivity and low methanol permeability. *Adv. Mater.* **2018**, *30*, 1705155.
(45) Yu, J.; Cui, Y.; Xu, H.; Yang, Yu.; Wang, Z.; Chen, B.; Qian, G. Confinement of pyridinium hemicyanine dye within an anionic metal-organic framework for two-photon-pumped lasing. *Nat. Commun.* **2013**, *4*, 2719.
(46) Wang, Z.; Zhu, C.-Y.; Mo, J.-T.; Fu, P.-Y.; Zhao, Y.-W.; Yin, S.-Y.; Jiang, J.-J.; Pan, M.; Su, C.-Y. White-light emission from dual-way photon energy conversion in a dye-encapsulated metal-organic framework. *Angew. Chem., Int. Ed.* **2019**, *58*, 9752−9757.
(47) Sun, Q.; Aguila, B.; Lan, P. C.; Ma, S. Tuning pore heterogeneity in covalent organic frameworks for enhanced enzyme accessibility and resistance against denaturants. *Adv. Mater.* **2019**, *31*, 1900008.
(48) Liang, W.; Carraro, F.; Solomon, M. B.; Bell, S. G.; Amenitsch, H.; Sumby, C. J.; White, N. G.; Falcaro, P.; Doonan, C. J. Enzyme encapsulation in a porous hydrogen-bonded organic framework. *J. Am. Chem. Soc.* **2019**, *141*, 14298−14305.
(49) Zhou, Y.; Jiang, L. Bioinspired nanoporous membrane for salinity gradient energy harvesting. *Joule* **2020**, *4*, 2244−2248.
(50) Logan, B. E.; Elimelech, M. Membrane-based processes for sustainable power generation using water. *Nature* **2012**, *488*, 313−319.
(51) Zhang, Z.; Yang, S.; Zhang, P.; Zhang, J.; Chen, G.; Feng, X. Mechanically strong MXene/Kevlar nanofiber composite membranes as high-performance nanofluidic osmotic power generators. *Nat. Commun.* **2019**, *10*, 2920.
(52) Ding, L.; Xiao, D.; Lu, Z.; Deng, J.; Wei, Y.; Caro, J.; Wang, H. Oppositely charged $Ti_3C_2T_x$ MXene membranes with 2D nanofluidic channels for osmotic energy harvesting. *Angew. Chem., Int. Ed.* **2020**, *59*, 8720−8726.
(53) Xiao, K.; Giusto, P.; Wen, L.; Jiang, L.; Antonietti, M. Nanofluidic ion transport and energy conversion through ultrathin free-Standing polymeric carbon nitride membranes. *Angew. Chem., Int. Ed.* **2018**, *57*, 10123−10126.
(54) Cheng, H.; Zhou, Y.; Feng, Y.; Geng, W.; Liu, Q.; Guo, W.; Jiang, L. Electrokinetic energy conversion in self-assembled 2D nanofluidic channels with Janus nanobuilding blocks. *Adv. Mater.* **2017**, *29*, 1700177.
(55) Zhang, Z.; He, L.; Zhu, C.; Qian, Y.; Wen, L.; Jiang, L. Improved osmotic energy conversion in heterogeneous membrane boosted by three-dimensional hydrogel interface. *Nat. Commun.* **2020**, *11*, 875.
(56) Feng, J.; Graf, M.; Liu, K.; Ovchinnikov, D.; Dumcenco, D.; Heiranian, M.; Nandigana, V.; Aluru, N. R.; Kis, A.; Radenovic, A. Single-layer MoS_2 nanopores as nanopower generators. *Nature* **2016**, *536*, 197−200.
(57) Chen, C.; Liu, D.; He, L.; Qin, S.; Wang, J.; Razal, J. M.; Kotov, N. A.; Lei, W. Bio-inspired nanocomposite membranes for osmotic energy harvesting. *Joule* **2020**, *4*, 247−261.
(58) Sun, Y.; Dong, T.; Lu, C.; Xin, W.; Yang, L.; Liu, P.; Qian, Y.; Zhao, Y.; Kong, X.-Y.; Wen, L.; Jiang, L. Tailoring a poly(ether sulfone) bipolar membrane: osmotic-energy generator with high power density. *Angew. Chem., Int. Ed.* **2020**, *59*, 17423−17428.
(59) Lin, C.-Y.; Combs, C.; Su, Y.-S.; Yeh, L.-H.; Siwy, Z. S. Rectification of concentration polarization in mesopores leads to high conductance ionic diodes and high performance osmotic power. *J. Am. Chem. Soc.* **2019**, *141*, 3691−3698.
(60) Zhu, C.; Liu, P.; Niu, B.; Liu, Y.; Xin, W.; Chen, W.; Kong, X.-Y.; Zhang, Z.; Jiang, L.; Wen, L. Metallic two-dimensional MoS_2 composites as high-performance osmotic energy conversion membranes. *J. Am. Chem. Soc.* **2021**, *143*, 1932−1940.
(61) Siria, A.; Poncharal, P.; Biance, A.-L.; Fulcrand, R.; Blase, X.; Purcell, S. T.; Bocquet, L. Giant osmotic energy conversion measured in a single transmembrane boron nitride nanotube. *Nature* **2013**, *494*, 455−458.
(62) Uribe-Romo, F. J.; Hunt, J. R.; Furukawa, H.; Klöck, C.; O'Keeffe, M.; Yaghi, O. M. A crystalline imine-linked 3-D porous covalent organic framework. *J. Am. Chem. Soc.* **2009**, *131*, 4570−4571.
(63) Catania, K. The shocking predatory strike of the electric eel. *Science* **2014**, *346*, 1231−1234.
(64) Huang, W.-L.; Wang, X.-D.; Ao, Y.-F.; Wang, Q.-Q.; Wang, D.-X. Artificial chloride-selective channel: shape and function mimic of the ClC channel selective pore. *J. Am. Chem. Soc.* **2020**, *142*, 13273−13277.
(65) Rollings, R. C.; Kuan, A. T.; Golovchenko, J. A. Ion selectivity of graphene nanopores. *Nat. Commun.* **2016**, *7*, 11408.

https://doi.org/10.1021/jacs.1c02090
J. Am. Chem. Soc. 2021, 143, 9415−9422

(66) Lee, C.; Joly, L.; Siria, A.; Biance, A.-L.; Fulcrand, R.; Bocquet, L. Large apparent electric size of solid-state nanopores due to spatially extended surface conduction. *Nano Lett.* **2012**, *12*, 4037−4044.
(67) Duan, C.; Majumdar, A. Anomalous ion transport in 2-nm hydrophilic nanochannels. *Nat. Nanotechnol.* **2010**, *5*, 848−852.

https://doi.org/10.1021/jacs.1c02090
J. Am. Chem. Soc. 2021, 143, 9415−9422